Kinematically-isolated diffuse starlight traces cluster dark matter cores

Callum Bellhouse[1], Steven P Bamford[1*], Nina A Hatch[1], Tutku Kolcu[1], Johan Richard[2]

[1*]School of Physics and Astronomy, University of Nottingham, Nottingham, NG7 2RD, UK.
[2]Centre de Recherche Astrophysique de Lyon UMR5574, 69230 Saint-Genis-Laval, France.

*Corresponding author(s). E-mail(s): steven.bamford@nottingham.ac.uk;
Contributing authors: callum.bellhouse@nottingham.ac.uk; nina.hatch@nottingham.ac.uk; tutku.kolcu@nottingham.ac.uk; johan.richard@univ-lyon1.fr;

Abstract

Dark matter governs the formation of the largest structures, yet remains poorly understood. Promising insights are offered by measurements of the central profile of dark matter haloes, but current constraints are inconclusive. In galaxy clusters, intracluster light (ICL) offers a novel tracer of dark matter, but is difficult to distinguish from the brightest cluster galaxy (BCG). We resolve this by using integral-field spectroscopy to kinematically isolate the ICL in AS1063 and map its spatial distribution and line-of-sight kinematics. Within 100 kpc, the ICL contains a stellar mass comparable to that of the BCG, exhibits a constant velocity dispersion, and follows a surface-brightness profile that matches independent estimates of the dark matter density distribution. Unique to our approach, we measure both spatial and kinematic offsets between the BCG and ICL, suggesting the BCG is oscillating around the cluster centre. Together, these results favour a cored dark matter density profile, in tension with the standard cold dark matter model. This work establishes kinematically isolated ICL as a sensitive dynamical probe of cluster halo cores and hence the nature of dark matter.

1 Introduction

Dark matter, an invisible component inferred only through its gravitational effects, underpins our current understanding of galaxies and the large-scale structure of the Universe, even though its fundamental nature remains elusive. In cosmological simulations, including dark matter results in the assembly of distinct halos in the early Universe, which subsequently merge in a hierarchical fashion. This behaviour is essential for reproducing the statistics of the observed galaxy distribution. The prevailing model, known as cold dark matter (CDM), features slow-moving particles that interact only gravitationally with themselves and ordinary matter. However, several alternative models – including warm, mixed, fuzzy, and self-interacting dark matter (SIDM) – can also match existing observations. A promising way to distinguish among these scenarios is to examine the inner regions of dark matter halos, since the additional physical processes in many alternative models alter the central structure of halos, producing 'cored' mass distributions, with shallow central density profiles compared to the sharply-peaked, 'cuspy', profiles formed in standard CDM [1].

The most massive dark matter halos host galaxy clusters, which typically contain a dominant central brightest cluster galaxy (BCG), surrounded by hundreds of less massive satellite galaxies and a diffuse stellar component known as the intracluster light (ICL). Although some stars form from gas cooling in the centre of the main halo, the majority of stars in the BCG and ICL are formed in other halos and later assembled into these structures through mergers and tidal stripping. Stars that lose orbital energy sink toward the centre, where baryons dominate the mass density, and become part of the BCG. Stars that remain on higher-energy orbits populate the extended ICL, where the gravitational potential is determined primarily by dark matter. The ICL stars can thus be considered bound to the cluster halo as a whole rather than to the BCG, suggesting that the ICL may trace the underlying dark matter potential.

Observational evidence already supports this picture. Gravitational lensing measurements indicate that, in the outskirts of clusters, the isophotes of the diffuse stellar light closely follow the contours of the total mass distribution [2]. Spectroscopy of the integrated stellar light [3–5] and of discrete tracers such as planetary nebulae [6, 7] reveals radially rising velocity-dispersion profiles, consistent with an extended stellar component whose dispersion approaches that of the cluster dark matter halo. Isolating the properties of the ICL throughout the cluster would provide a powerful tracer of the full halo potential, enabling constraints on the inner density profile and discrimination between dark matter models. To date, however, disentangling the BCG from the surrounding ICL has proved challenging. There is no consensus theoretical definition of the boundary between the two components, and observationally they blend smoothly in surface brightness and morphology. This has limited our ability to extend ICL-based constraints from the outskirts into the inner regions of the halo, where different dark matter models diverge most strongly.

To overcome this difficulty, we exploit the fact that cosmological simulations predict that the most striking difference between the BCG and the ICL lies in their stellar kinematics, with the ICL exhibiting higher velocity dispersions and more weakly bound orbits than the BCG stars [8, 9]. To measure these kinematics, we turn to spatially resolved spectroscopy using an integral-field spectrograph. Spectroscopy also provides

additional, powerful diagnostic information: if the two components host different stellar populations, this will be reflected both in the overall continuum shape (analogous to broadband colours) and in the strengths of key absorption features. Here we show that combining kinematic and stellar-population diagnostics allows us to separate the BCG and ICL robustly, and to measure the radial distribution and kinematics of the ICL over radii 5–100 kpc from the halo centre, thereby probing the inner dark matter potential.

2 Results

Our target is AS1063, a massive galaxy cluster at $z = 0.348$ [10] with a mass $M_{200} \approx 2.5 \times 10^{15}\, M_{\odot}$ [11]. It is an ideal system for demonstrating our new method, since the large number of strongly-lensed background sources allows the dark matter distribution in the core to be independently estimated (e.g. [12, 13]). We use integral-field spectroscopy from the Multi Unit Spectroscopic Explorer (MUSE [14]) instrument covering the central 300×600 kpc of the cluster. We complement these data with Hubble Space Telescope (HST) Frontier Fields WFC3 images, from which we construct a high-fidelity mask that we applied to the MUSE data to exclude spatial bins contaminated by sources other than the BCG and ICL. After a careful background subtraction, the masked MUSE data are adaptively binned on the sky to increase sensitivity in low-surface-brightness regions while maintaining high spatial resolution in the bright cluster centre (see Section 3 for details).

We employ pPXF [15] to fit the spectrum of each spatial bin, using stellar population models convolved by a line-of-sight velocity distribution (LOSVD) with the standard Gauss–Hermite parametrization [16]. A fit with a single kinematic component produces a LOSVD with a dispersion that increases with radius and which exhibits significant positive kurtosis, particularly at radii of ∼30 kpc (see Section 3 and fig. ED2). This behaviour is consistent with a superposition of a low-dispersion stellar population and a more spatially extended, higher-dispersion population. This motivates fitting the spectra with two distinct kinematic components, which we identify with the BCG and ICL.

The signal-to-noise ratio of the data is insufficient to robustly fit two stellar components with fully independent kinematics and stellar populations. We therefore make the simplifying assumption that the BCG and the ICL can each be represented by a single, fixed stellar population. The ICL template is constructed by determining the SSP weights from a pPXF fit to the spectrum integrated over a 50–100 kpc annulus, where the BCG contribution is expected to be negligible. Similarly, the BCG template is derived from a region within 5 kpc of the BCG centre, taking care to account for potential ICL contamination. See Section 3, and figs. ED3 and ED1 for details.

The stellar populations inferred for both the central and outer regions formed at very early times. However, the mean metallicity of the BCG population is super-solar, whereas that of the ICL is a factor of 1.6 lower, around solar. This is consistent with previous studies of the ICL metallicity [17] and suggests that the BCG stars predominantly formed in the centres of massive galaxies, while the ICL stars originate mainly in low-mass systems or the outskirts of massive galaxies.

We now model the spectrum of each bin as the sum of two kinematic components with independent velocities, dispersions, and relative weights, whose stellar populations are fixed to the BCG and ICL templates, respectively.

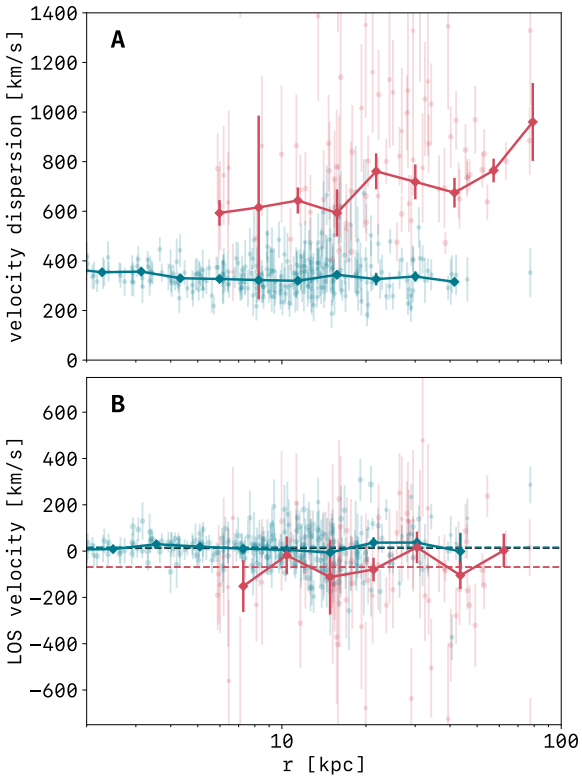

Fig. 1 The kinematics of the BCG and ICL components versus clustercentric radius. The velocity dispersion (**A**) and line-of-sight velocity (**B**) of the BCG (blue) and ICL (red), from two-component fits to our spatially-binned MUSE data. Small points show the pPXF measurement, with its uncertainty, for the individual spatial bins. To ensure our kinematic decomposition is robust, we only consider bins where the total (BCG+ICL) surface brightness is brighter than 25 mag arcsec^{-2} and the uncertainty on the velocity dispersion is less than one third of its measured value. The large diamonds show the error-weighted mean value in logarithmic bins of radius, with error bars indicating the standard error within each radial bin. The dashed lines in panel **B** indicate the error-weighted mean velocities of each component.

We show in fig. 1A that the kinematic component corresponding to the BCG stellar population has an almost flat velocity-dispersion profile at all radii, with a mean value of 335 ± 4 km s^{-1}. The ICL component likewise displays an approximately flat velocity-dispersion profile, with a mean of 690 ± 30 km s^{-1}. This is close to the value expected from simulations, for intracluster stars at radii of $\sim$100 kpc [18]. The measured dispersion is somewhat lower than that of the cluster galaxy population, since intracluster stars occupy less energetic orbits than the bulk of the dark matter [19]. The near constancy of both dispersions over an order of magnitude in radius

strengthens our picture of a dynamically hot ICL component that penetrates into the inner regions of the cluster while continuing to trace the cluster's large-scale mass distribution. In addition to the differing velocity dispersions, the two components are also offset in line-of-sight velocity (see Fig. 1B), with the BCG moving at $86 \pm 18\,\mathrm{km\,s^{-1}}$ relative to the ICL.

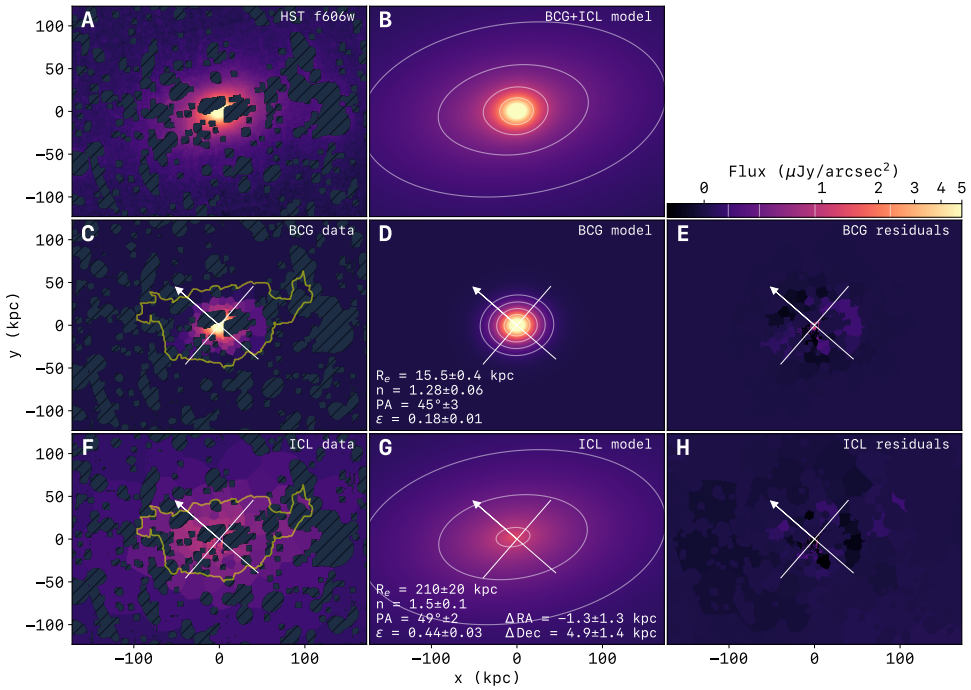

Fig. 2 The distribution of the BCG and ICL in each spatial bin of the MUSE datacube. **A**: HST F606W image smoothed with a Gaussian of width $\sigma = 0.55$ arcsec to mimic the seeing of the MUSE observations; all sources other than the BCG and ICL are masked (gray regions). **B**: The total BCG+ICL light obtained by summing the individual models shown in panels D and G. **C**: Image constructed from the MUSE data showing the light attributed to the BCG in each spatial bin. The yellow contour encloses bins brighter than $25\,\mathrm{mag\,arcsec^{-2}}$, for which we can separate the BCG and ICL components; beyond this we assign all the MUSE flux to the ICL. The arrow points North, and East is anticlockwise. **D**: Sérsic model for the BCG light in panel C. Best-fit values and 1σ uncertainties are given for the half-light radius (R_e), Sérsic index (n), position angle (PA; degrees East of North), and ellipticity ($\epsilon = 1 - b/a$). **E**: Residuals between the BCG model (panel D spatially-binned) and the data in panel C. **F**: As panel C, but showing the light attributed to the ICL in each spatial bin. **G**: Sérsic model for the ICL light in panel F. RA and Dec offsets are given relative to the BCG, defining West as positive. **H**: Residuals between the ICL model (panel G spatially-binned) and the data in panel F.

We next explore the spatial distribution of the ICL and BCG components. To improve the robustness of the ICL fluxes in the cluster centre, where the BCG dominates, we perform a second set of PPXF fits in which the kinematics (dispersion and line-of-sight velocity) of each component are fixed to their average values derived

above. We reconstruct a flux-calibrated spectrum for each component in every spatial bin, and convolve these spectra with the HST/WFC3 F606W response curve to obtain the decomposed BCG and ICL surface brightness in each bin. The resulting surface brightness maps (panels C and F of Fig. 2) reveal that the BCG and ICL components have contrasting spatial distributions. This is even clearer in the one-dimensional surface brightness profiles shown in Fig. 3. Note that, apart from defining the BCG and ICL templates from the central and outer regions of the MUSE field, we do not impose any prior spatial distribution on either component. We find that the BCG dominates the light within 25 kpc, with the light beyond 50 kpc being entirely ICL. Nevertheless, the surface brightness of the ICL component increases monotonically toward the centre of the cluster. Even though the BCG component is 2.5 mag brighter at a radius of $\sim$5 kpc, we still significantly detect the presence of an ICL component.

Our kinematically constrained ICL profile differs markedly from the photometric decomposition of this system by [20], who attribute considerably more light to the BCG at all radii. Within 100 kpc we find that 55% of the BCG+ICL stellar mass belongs to the ICL, significantly larger than the 29% inferred from the photometric analysis. Within the full extent of our observations, which reaches 300 kpc beyond the BCG, the ICL constitutes 65% of the *total* stellar mass (i.e. including other galaxies) within this radius, compared to the 23% obtained from their purely photometric decomposition [20]. Our method shows, for the first time in observations, but as predicted by simulations [21], that photometric measures of the ICL underestimate the amount of stars that orbit in the cluster halo, rather than being bound to any particular galaxy.

To quantify the spatial structure of the BCG and ICL, we fit two-dimensional elliptical Sérsic profiles to their surface brightness distributions, using a modified version of the AstroPhot package [22] adapted to fit the spatially binned maps (see Section 3). The resulting models for the BCG and ICL are shown in panels D and G of Fig. 2, and their sum (panel B) reproduces the masked HST image (panel A) remarkably well. Although the ICL flux in each bin is determined independently, its two-dimensional distribution is nonetheless well described, over an order of magnitude in radius, by a single elliptical Sérsic profile. This inspires confidence that these fits provide tight constraints on the radial profile, ellipticity and projected centre of the ICL.

The BCG has a half-light radius of 15.5 ± 0.4 kpc and an ellipticity of 0.18 ± 0.01, typical of massive cluster elliptical galaxies [23, 24]. By contrast, the ICL is more extended and elongated, with a half-light radius of 210 ± 20 kpc, and ellipticity 0.44 ± 0.03, and its centroid is offset from the BCG by 5.2 ± 1.5 kpc.

Because our goal is to use the ICL as a tracer of the dark matter distribution, we compare its shape, centroid and radial profile with those of the dark matter distribution inferred from strong gravitational lensing [12]. Although strong lensing has its own limitations [**?**], it is currently accepted as the best tool we have to estimate the distribution of dark matter in individual clusters.

The position angle of the ICL is consistent, within the uncertainties, with that of the lensing-derived dark matter halo (table 5 of [12]). The ICL is significantly rounder (ellipticity $\epsilon = 0.44$) than the dark matter halo ($\epsilon = 0.6$) in the lensing model, in contrast with findings by [25] that the ICL halos of relaxed simulated clusters are typically more elongated than their dark matter halos, albeit with a large scatter.

However, the dark matter model of AS1063 assumes a single ellipticity for the entire cluster, whereas simulations indicate that dark matter cores are typically rounder than halo outskirts [26], which may explain this discrepancy. The detected centroid offset of the ICL from the BCG, of 1.3 ± 1.3 kpc East and 4.9 ± 1.4 kpc North, is similar to the offset of the lensing mass centroid, 2.5 ± 1.1 kpc East and 2.6 ± 0.7 kpc North. In summary, the ICL shape and centroid closely match the strong-lensing estimate of the underlying dark matter halo, with the rounder ICL ellipticity plausibly closer to the true shape of the inner halo. This supports the view that isolating the ICL from the BCG allows us to probe the two-dimensional shape of the cluster's central dark matter potential.

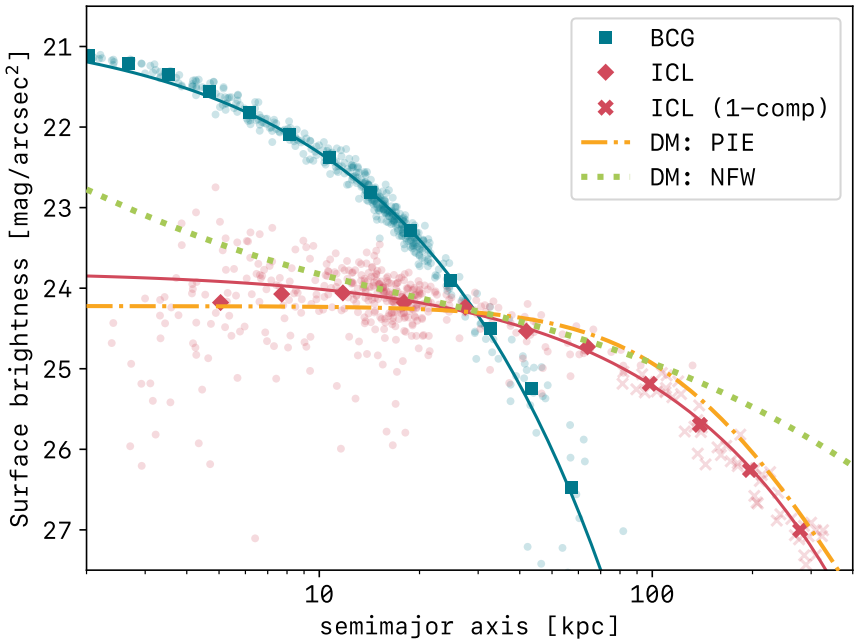

Fig. 3 One-dimensional surface-brightness profiles of the BCG and ICL. The surface brightness of each component in the MUSE spectra convolved with the HST/F606W transmission curve, plotted against the semimajor axis of the isophote that passes through the point. The values for each spatial bin are shown as small blue (BCG) and red (ICL) points. Large symbols show the mean values in logarithmic bins of the semimajor axis. The solid curves show a one-dimensional Sérsic fit to the large points for each component. Crosses indicate bins where we assign all the flux to the ICL. Over-plotted are two dark matter surface mass profiles that are normalised to the ICL at 30 kpc, a pseudo-isothermal ellipse (PIE) profile with a core radius of 100 kpc, and a NFW profile with an inner slope of $\gamma = 1$. The ICL is a close match to the cored, pseudo-isothermal model.

Turning to the radial profile, our constraints on the ICL light profile and kinematics together point to a total mass distribution that is well described by a cored halo. Fig. 3 illustrates that the ICL profile within the inner $\sim$300 kpc closely matches the shape of the dark matter profile estimated by strong lensing. Furthermore, the ICL velocity dispersion is high ($\sim$690 km s^{-1}) and approximately flat from 5 to 100 kpc, indicating that the inner potential varies only slowly with radius. Both signatures strongly support a cored dark matter halo in this cluster. This is consistent with the strong-lensing analysis of [12], which favours a pseudo-isothermal halo with a $\sim$100 kpc core over a cuspy NFW [27] profile.

Further evidence that the centre of this cluster has a relatively flat density profile comes from the observed offset in phase space (5.2 ± 1.5 kpc and 86 ± 18 km s^{-1}) between the ICL and the BCG. This indicates that, while the BCG is bound to the cluster core, it nonetheless oscillates within a relatively broad minimum of the dark matter potential. While such oscillations are expected if the cluster has experienced a recent merger, they would be rapidly damped by the cuspy core predicted in standard CDM, but can persist for longer in a cored dark matter halo. The method we have set out in this article is the only way to determine accurate offsets between the BCG and the large-scale dark matter halo in *phase-space*. Other methods only measure projected spatial offset. This is particularly valuable, as an anti-correlation between the spatial and velocity offsets is a hallmark of harmonic oscillation, and hence the presence of a cored halo [28]. The single detection presented here does not, by itself, pose a challenge to CDM; however, if the majority of clusters were found to exhibit BCG oscillations of the kind we have demonstrated here, this would favour alternative dark matter models [1].

By combining spatially-resolved spectroscopy with stellar-population modelling, our results demonstrate that the intracluster light in AS1063 can be isolated kinematically from the BCG, mapped throughout the central region of the cluster, and used as a precise tracer of the inner dark matter halo. We show that the ICL forms a dynamically hot, extended component whose shape, centroid and velocity dispersion closely track the total mass distribution, distinct from the compact, metal-rich BCG that inhabits the cluster centre. The ICL's flat surface-brightness and velocity-dispersion profiles, and the small but significant BCG-ICL phase-space offset, all point to a cored rather than cuspy central dark matter density profile in this cluster. If similar kinematic decompositions across a statistical sample of clusters reveal that such cores and BCG 'wobbles' are common, this would provide a new avenue for testing CDM against alternative dark matter models. More broadly, our approach shows that the diffuse stellar component in clusters is not merely a by-product of galaxy assembly, but a powerful dynamical probe of the central potential, opening a complementary route – alongside lensing and X-ray studies – to mapping the distribution and nature of dark matter on cluster scales.

3 Methods

Data processing

Datasets

We use integral-field spectroscopy from the MUSE [14] instrument on the Very Large Telescope (VLT). The observations comprise two pointings on AS1063 that cover the North-East and South-West regions [29, 30] (see fig. ED1). Total on-source integration times are 4.8 h (NE) and 3.1 h (SW). For this analysis we reprocessed the observations and omitted the autocalibration step to preserve low-surface-brightness structure in the intracluster light (ICL).

We complement the spectroscopy with HST Frontier Fields WFC3 imaging in F435W, F606W, and F814W, processed as in [31]. These images provide higher spatial resolution and deeper limiting surface brightness than MUSE and are used to build the source mask applied to the MUSE cube.

Galaxy masking

To exclude light from cluster satellites and line-of-sight sources, we construct a mask from the deep HST images in multiple stages. To start, we smooth the images with a Gaussian of $\sigma = 0.55$ arcsec to mimic the atmospheric smoothing ('seeing') present in the MUSE data cube (this difference in spatial resolution can be seen when comparingt fig. ED1A and B). We subtract a two-dimensional median background from each HST image, then detect and deblend sources based on a 5σ excess relative to the background-subtracted image. The resulting sources, except the BCG, form the first mask. We next apply a stricter background subtraction (smaller box size) to capture spatial variations within the ICL region. Sources close to the BCG are again detected and deblended using a 5σ threshold. Additional source pixels identified in this pass (excluding the BCG) are added to the first mask. We then repeat this entire procedure with the original unsmoothed HST images, to locate smaller, fainter objects. We dilate this second mask by 0.72 arcsec to account for the seeing in the MUSE data. The final mask is formed by combining all the masks, then reprojected to the MUSE pixel scale and orientation, and applied to the data cube to remove all sources of light except the BCG and diffuse light. The final masked HST F606W image can be seen in Fig. 2A.

MUSE background subtraction

An initial background subtraction of the MUSE data cube was performed by the standard pipeline, which successfully removed contamination from sky lines. To investigate and correct for any residual background, we take the following steps. We first apply the galaxy mask, then additionally mask a central region defined by an ellipse ($\epsilon = 0.43$, PA $= 50$ deg) centred on the approximate BCG position at RA $= 342.183$, Dec $= -44.531$ with a semi-major axis of 200 kpc. This ellipse was measured from the smoothed HST F606W image using the isophotal fitting tool `autoprof` [22]. The shape of this extra mask is designed to conservatively exclude the region in which ICL is detectable. From the remaining unmasked regions, we create a white light image by integrating the flux over all wavelengths of the spectra and select the faintest 20% of

regions within the image. The spectra from these regions are averaged to construct a background spectrum. To verify the spatial uniformity of this background spectrum, we produce independent spectra from the four corners of the masked field and confirm no significant differences between them. The global background spectrum is fit with a 4th-order polynomial, which is then subtracted from every spectrum in the cube.

Voronoi binning

Because the ICL is extremely faint in individual spectra, we increase the signal-to-noise ratio (S/N) by combining spectra into spatial bins constructed using Voronoi tessellation following [32]. The two-pointing mosaic exhibits elevated noise along the central vertical join, which yields overly large bins if we target uniform S/N. Instead, we create Voronoi bins in which the square root of the total signal (flux integrated over all wavelengths) is constant. This yields a smoother distribution of bin sizes across the field-of-view, preserving higher spatial resolution in bright central regions, with larger bins at low surface brightness. The target flux is set by balancing adequate S/N in the faintest regions against retaining enough bins to resolve azimuthal structure in the ICL.

Spectral fitting

Single-component fits

We first fit the spectrum from each Voronoi bin with a single kinematic component parameterized by velocity v, dispersion σ, and Gauss-Hermite moments h_3 and h_4. Initial parameters are set to $v = 0\,\mathrm{km\,s^{-1}}$ (BCG rest frame), $\sigma = 400\,\mathrm{km\,s^{-1}}$, and $h_3 = h_4 = 0$. We use the full set of SMILES templates [33], including varying [α/Fe], to prioritize accurate recovery of the kinematics. The resulting radial dispersion profile (Fig. ED2A) is approximately flat at $\sim$350 $\mathrm{km\,s^{-1}}$ in the BCG-dominated centre, increases beyond $\sim$10 kpc, and then rises steeply from $\sim$600 $\mathrm{km\,s^{-1}}$ at $\sim$60 kpc to $\sim$1400 $\mathrm{km\,s^{-1}}$ by $\sim$100 kpc. The h_4 (kurtosis) profile (Fig. ED2B) peaks at $\sim$35 kpc, indicating a LOSVD with enhanced wings consistent with the superposition of a narrow (BCG-like) and a broad (ICL-like) component. These diagnostics motivate the subsequent approach of fitting multiple components to each Voronoi bin.

Empirical BCG and ICL templates

We construct empirical templates for the BCG and ICL stellar populations by extracting high S/N spectra in regions we expect to be dominated by a single component. The BCG spectrum is extracted within a 0–5 kpc circular aperture; the ICL spectrum is extracted from a 50–100 kpc elliptical annulus (with $\epsilon = 0.43$ and PA = 50 deg), after masking satellites and foreground/background objects. These regions are marked on fig. ED1B. We then fit these spectra using pPXF [15], with SSP templates that allow variation in [α/Fe] to mitigate template mismatch [33]. To avoid contaminating our BCG template with projected ICL, when fitting the spectrum for the central region we include an additional component with *fixed* stellar population and LOSVD defined by the fit to the ICL region. The observed high S/N spectra are shown in Fig. ED3, overlaid with the pPXF models.

The best-fitting stellar population templates indicate that the stellar population of both the ICL and BCG components are old: the ICL and BCG have luminosity–weighted ages of ∼9.3 and ∼9.6 Gyr, respectively. Their metallicities differ, with the BCG being metal–rich ($\langle[\mathrm{M/H}]\rangle = +0.26$) compared to the mildly supersolar ICL ($\langle[\mathrm{M/H}]\rangle = +0.048$). The inferred α–enhancements are similar, given the uncertainties, with the ICL and BCG yielding $\langle[\alpha/\mathrm{Fe}]\rangle \simeq +0.03$ and $\simeq 0.0$, respectively. This pattern – old populations, higher central metallicity, and comparable α–enhancement for core and diffuse components – is broadly consistent with the negative metallicity gradients and ancient stellar populations reported for BCGs and diffuse cluster light [e.g., [34–36]]. The consistent, near–solar $\langle[\alpha/\mathrm{Fe}]\rangle$ values fall within the range observed for massive BCGs and their halos [e.g., [37]], and may reflect similar enrichment timescales for the dominant progenitors of both components. The best-fitting stellar population templates indicate that the BCG has a mass-to-light ratio of $8.4\,\mathrm{M_\odot/L_\odot}$, whereas the ICL has a lower mass to light ratio of $5\,\mathrm{M_\odot/L_\odot}$.

Multi-component decomposition

Using the empirical templates, we fit the spectrum from each Voronoi bin with two kinematic components: one template is always fixed to the BCG stellar population and the other is fixed to the ICL stellar population template. The baseline model, used throughout the main article, contains BCG and ICL components with initial line-of-sight $v = 0\,\mathrm{km\,s^{-1}}$, and with initial dispersions of $\sigma_{\mathrm{BCG}} = 357$ and $\sigma_{\mathrm{ICL}} = 791\,\mathrm{km\,s^{-1}}$ (as measured from the high S/N BCG and ICL spectra used to construct the empirical stellar population templates). Bounds of $\pm 3000\,\mathrm{km\,s^{-1}}$ in velocity and 0–$2000\,\mathrm{km\,s^{-1}}$ in dispersion are imposed. We find that the decomposition becomes unreliable for spatial bins with a total surface brightness fainter than $25\,\mathrm{mag\,arcsec^{-2}}$, so only make use of bins brighter than this limit in our kinematic analysis. These bins are marked by a yellow contour in Fig. 2C and F. For defining this threshold, the total surface brightness in each bin is estimated by convolving our best-fitting single-component model (as described above) with the HST/F606W transmission curve.

The kinematic properties of the two components are shown in Fig. 1. To explore how different starting values can affect our results, we tested several different initial velocity dispersions for both components and find similar results.

To reduce the noise in our surface brightness estimates when creating the maps in Fig. 2, we perform a second decomposition in which we fix both the stellar population templates (BCG and ICL, as above) and also the kinematics. The BCG kinematics are fixed to a line-of-sight velocity of $v = 16\,\mathrm{km\,s^{-1}}$ and $\sigma_{\mathrm{BCG}} = 335\,\mathrm{km\,s^{-1}}$, and the ICL is fixed to $v = -69\,\mathrm{km\,s^{-1}}$ with $\sigma_{\mathrm{ICL}} = 691\,\mathrm{km\,s^{-1}}$. In these fits, only the relative weights of the two components are allowed to vary. We again limit our use of a two-component model to bins with a total surface brightness of at least $25\,\mathrm{mag\,arcsec^{-2}}$ averaged over the fig. ED1 filter. Although this second decomposition is more robust, at fainter surface brightness levels we find the contribution of the BCG is negligible (see Fig. 3). In fainter bins, we therefore set the BCG component to zero and estimate the ICL surface brightness from a single-component fit using the ICL template (with fixed kinematics).

Surface brightness fitting

In the HST images, diffuse ICL extends into the same region that we use to define our background spectrum. We therefore accept that our MUSE background correction will over-subtract some light from each spectrum. When performing the surface brightness fitting of the ICL, we counter this over-subtraction by adding a constant of $0.03\,\mu\mathrm{Jy\,arcsec^{-2}}$ into the modelled two-dimensional ICL distribution (Fig. 2F) before measuring its Sérsic parameters. This corresponds to the surface brightness of the ICL measured in the smoothed HST F606W image in the same region over which we estimate our MUSE background level. We do not add any constant to the BCG image (Fig. 2C), since Fig. 3 shows that the BCG surface brightness at such large radii is negligible.

We fit independent elliptical Sérsic models to the BCG and ICL surface brightness maps derived from the spectral decomposition. For each component, the free parameters are the centroid (ΔRA, ΔDec), ellipticity (ϵ), position angle (PA, measured in degrees East from North), half-light radius (R_e), and Sérsic index (n). We estimate the flux uncertainty in each Voronoi bin from the F606W-convolved MUSE data and scale it by the fraction of flux assigned to the component (BCG or ICL) in that bin. Handling the Voronoi-binned data required some small modifications to `AstroPhot`. After each trial model is sampled onto a regular pixel grid, it is binned to the same Voronoi tessellation as the data. The residuals are then determined for each Voronoi bin, and the optimization proceeds in the usual manner.

Stellar fraction in the ICL

We calculate the fraction of stellar mass within the intracluster component using the Sérsic models derived from the 2D surface brightness maps in fig. 2. Within a circular aperture of 100 kpc the ICL/BCG+ICL *light* fraction is 67%. We convert the measured amount of light in each component to stellar mass using the mass-to-light ratios from the template fitting above. Since the ICL has a lower mass-to-light ratio than the BCG ($5\,\mathrm{M_\odot/L_\odot}$ versus $8.4\,\mathrm{M_\odot/L_\odot}$), this reduces the ICL/BCG+ICL fraction to 55%.

To calculate the fraction of *total* stellar mass fraction in the ICL we need a measure of the stellar mass in the galaxy population beyond the BCG. For this we use the galaxy stellar mass calculated by [20], who use the same initial mass function that we use in this work. We limit our stellar mass fraction to the maximum radius of our observations, i.e., 300 kpc. Within 300 kpc, [20] measure a total stellar mass of $9.8 \times 10^{11}\,\mathrm{M_\odot}$ within galaxies (other than the BCG). Within this radius, the BCG emits $1.8 \times 10^{11}\,\mathrm{L_\odot}$ from $1.5 \times 10^{12}\,\mathrm{M_\odot}$ of stars, whereas the ICL emits $9.1 \times 10^{11}\,\mathrm{L_\odot}$ from $4.5 \times 10^{12}\,\mathrm{M_\odot}$ of stars. Thus, the ICL constitutes 65% of the total stellar mass within 300 kpc of the cluster core.

Declarations

Funding. N.A.H. and T.K. were funded by the Leverhulme Trust through RLA-2022-002. C.B., N.A.H. and S.P.B. were funded by the UK Science and Technology Facilities Council (STFC) under grant ST/X000982/1.

Competing interests. There are no competing interests to declare.

Ethics approval and consent to participate. Not applicable

Consent for publication. Not applicable

Data, materials and availability. The MUSE IFU data underlying this article can be accessed from the ESO public archive (archive.eso.org/scienceportal) and the HST image data can be accessed from the public Frontier Fields archive (archive.stsci.edu/prepds/frontier). The derived data generated in this research will be shared on reasonable request to the corresponding author.

Author contributions. C.B., S.P.B. and N.A.H. collaboratively developed the core scientific ideas presented in this work, refined the analysis methodology and visualization of the results, and iterated on writing the final article. C.B. led the development of the spectral fitting and multicomponent decomposition pipeline, including measurements of the decomposed ICL and BCG kinematics, and extraction of surface brightness maps and profiles. S.P.B. developed the method for performing Sérsic fits to Voronoi-binned surface brightness maps. N.A.H. and S.P.B. acquired financial support for this project. T.K. performed isophotal fitting of the HST images and contributed comments on the final article. J.R. performed the initial processing of the MUSE datacubes.

Extended Data Figures

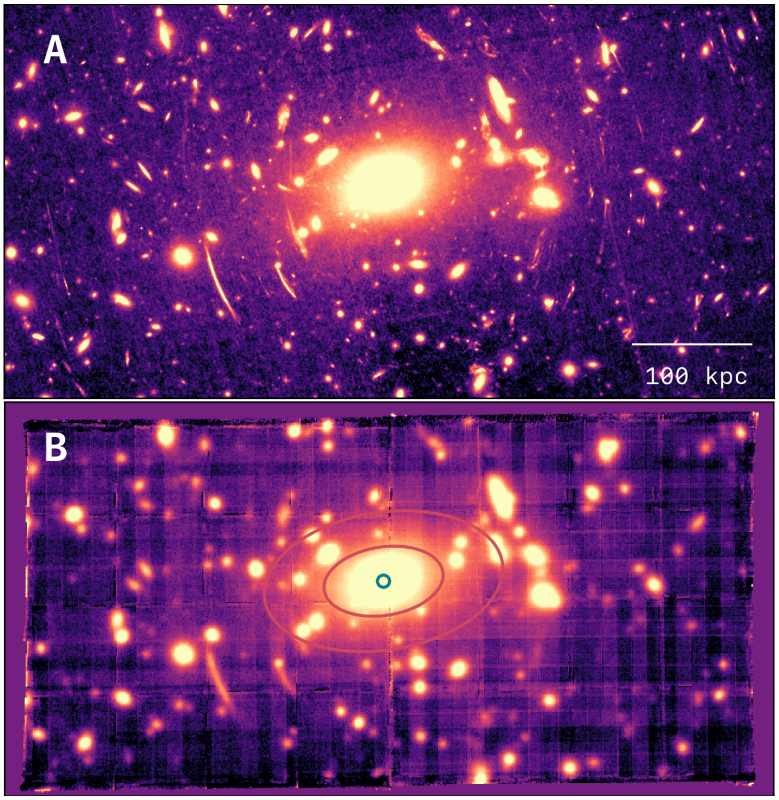

Fig. ED1 Comparison between the HST and MUSE images, illustrating regions in which template spectra are extracted. A: The HST F606W image, scaled to highlight the diffuse ICL emission. **B**: The MUSE image produced by convolving the spectra with the response curve of the F606W filter. The red ellipses and blue circle show the bounds of the regions used to calculate the template ICL (50–100 kpc elliptical annulus) and BCG (0–5 kpc circular aperture) spectra respectively.

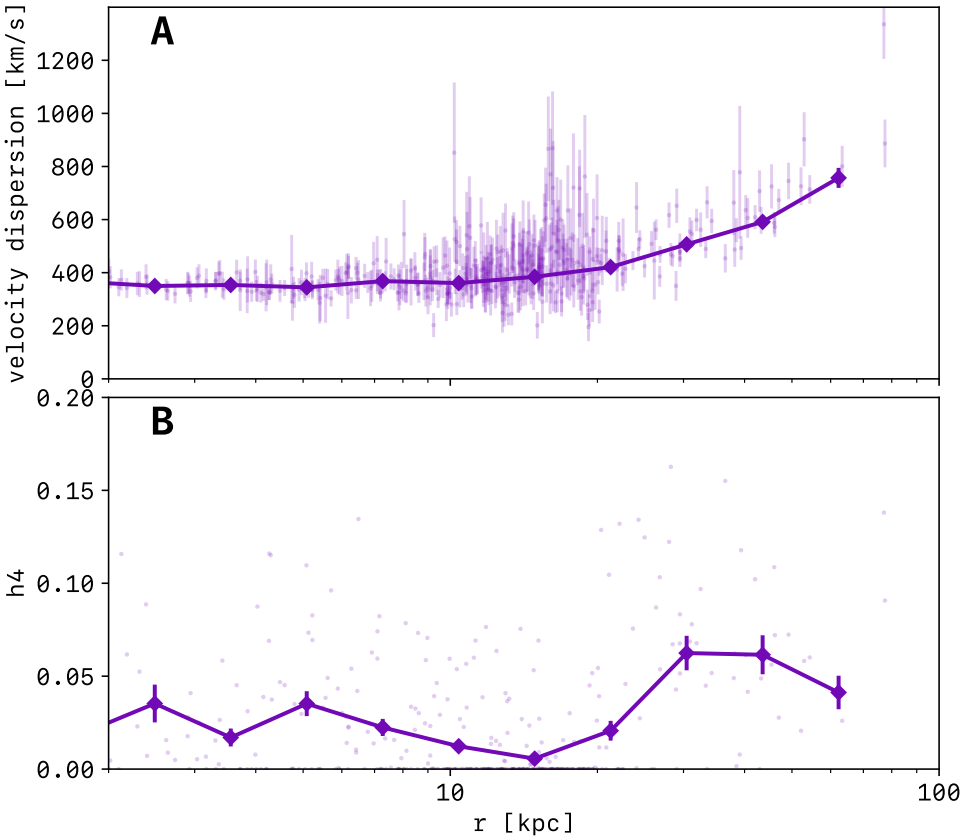

Fig. ED2 Velocity dispersion and h4 moment profiles for pPXF fits with a single kinematic component. Small points show the velocity dispersion (**A**) and the h_4 coefficient, or kurtosis, (**B**) of the LOSVD from the fit to the integrated spectrum in each Voronoi bin, versus the average radius of the spaxels within that bin. In panel A, error bars indicate the uncertainty reported by pPXF for each bin. To ensure reliable kinematics, we only consider bins where the total (BCG+ICL) surface brightness is brighter than $25\,\mathrm{mag\,arcsec^{-2}}$. The large diamonds and lines show the error-weighted mean value in logarithmic bins of radius, with error bars indicating the standard error within each radial bin.

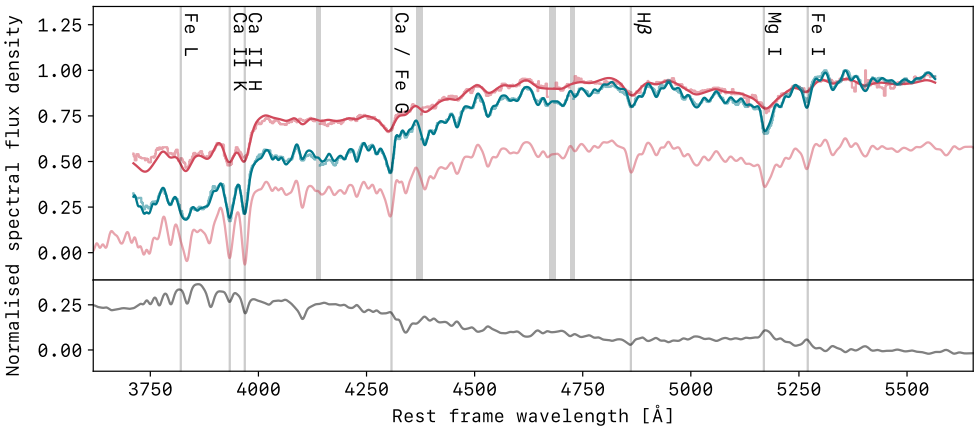

Fig. ED3 Construction of the BCG and ICL template spectra. The stepped lines show the MUSE integrated spectra, with 2× spectral binning, of the BCG (blue) and ICL (red) within the regions shown in fig. ED1. The solid curves show the pPXF fits to the spectra, which represent the best-fit combination of stellar templates convolved with the LOSVD of the integrated spectra. The faint red line shows the best-fit template spectrum of the ICL convolved with the LOSVD of the BCG, offset down by 0.5 in normalized flux, to facilitate comparison between the components. The gray lines mark the wavelengths of prominent absorption lines, while gray shaded regions mark the locations of masked sky lines. The bottom insert (grey line) shows the residual between the ICL and BCG best-fit templates, convolved with the LOSVD of the BCG.

References

[1] Harvey, D., Robertson, A., Massey, R., McCarthy, I.G.: Observable tests of self-interacting dark matter in galaxy clusters: BCG wobbles in a constant density core. Monthly Notices of the Royal Astronomical Society **488**(2), 1572–1579 (2019) arXiv:1812.06981 [astro-ph.CO]

[2] Montes, M., Trujillo, I.: Intracluster light as a luminous tracer of dark matter in galaxy clusters. Monthly Notices of the Royal Astronomical Society **482**(2), 2838–2851 (2019)

[3] Kelson, D.D., Zabludoff, A.I., Williams, K.A., Trager, S.C., Mulchaey, J.S., Bolte, M.: Determination of the dark matter profile of abell 2199 from integrated starlight. The Astrophysical Journal **576**(2), 720–734 (2002)

[4] Bender, R., Kormendy, J., Cornell, M.E., Fisher, D.B., Fabricius, M.H., Nowak, N., Thomas, J.: Structure and formation of cd galaxies: Ngc 6166 in abell 2199. The Astrophysical Journal **807**(1), 56 (2015)

[5] Gu, M., Conroy, C., Law, D., van Dokkum, P., Yan, R., Wake, D., Bundy, K., Villaume, A., Abraham, R., Merritt, A., Zhang, J., Bershady, M., Bizyaev, D., Drory, N., Pan, K., Thomas, D., Weijmans, A.-M.: Spectroscopic Constraints on the Buildup of Intracluster Light in the Coma Cluster. The Astrophysical Journal **894**(1), 32 (2020)

[6] Longobardi, A., Arnaboldi, M., Gerhard, O., Mihos, J.C.: The outer regions of the giant virgo galaxy m87: Kinematic separation of halo and intracluster light. Astronomy & Astrophysics **579**, 135 (2015)

[7] Hartke, J., Arnaboldi, M., Gerhard, O., Coccato, L., Merrifield, M., Kuijken, K., Pulsoni, C., Agnello, A., Bhattacharya, S., Spiniello, C., Cortesi, A., Freeman, K.C., Napolitano, N.R., Romanowsky, A.J.: The halo of M 105 and its group environment as traced by planetary nebula populations. II. Using kinematics of single stars to unveil the presence of intragroup light around the Leo I galaxies NGC 3384 and M 105. Astronomy & Astrophysics **663**, 12 (2022) arXiv:2201.08710 [astro-ph.GA]

[8] Dolag, K., Murante, G., Borgani, S.: The origin and properties of intracluster stars in a λcdm universe. Monthly Notices of the Royal Astronomical Society **405**(3), 1544–1559 (2010)

[9] Remus, R.-S., Burkert, A., Dolag, K.: The separation of brightest cluster galaxy and intracluster light in simulations. Monthly Notices of the Royal Astronomical Society **464**(3), 3742–3756 (2017)

[10] Gómez, P.L., *et al.*: Rxc j2248.7-4431: X-ray properties and dynamical state. Astronomy & Astrophysics **541**, 43 (2012)

[11] Rodriguez, A., Miller, C.J., Halenka, V., Kremin, A.: Escape Velocity Mass of A1063. The Astrophysical Journal **968**(1), 35 (2024) arXiv:2406.01330 [astro-ph.CO]

[12] Caminha, G.B., Grillo, C., Rosati, P., Balestra, I., Karman, W., Lombardi, M., Mercurio, A., Nonino, M., Tozzi, P., Zitrin, A., Biviano, A., Girardi, M., Koekemoer, A.M., Melchior, P., Meneghetti, M., Munari, E., Suyu, S.H., Umetsu, K., Annunziatella, M., Borgani, S., Broadhurst, T., Caputi, K.I., Coe, D., Delgado-Correal, C., Ettori, S., Fritz, A., Frye, B., Gobat, R., Maier, C., Monna, A., Postman, M., Sartoris, B., Seitz, S., Vanzella, E., Ziegler, B.: CLASH-VLT: A highly precise strong lensing model of the galaxy cluster RXC J2248.7-4431 (Abell S1063) and prospects for cosmography. Astronomy and Astrophysics **587**, 80 (2016) arXiv:1512.04555 [astro-ph.CO]

[13] Beauchesne, B., Clément, B., Limousin, M., Alcalde Pampliega, B., Jauzac, M., Niemiec, A., Richard, J., Mahler, G., Diego, J.M., Hibon, P., Koekemoer, A.M., Connor, T., Kneib, J.-P., Faisst, A.L.: A comprehensive separation of dark matter and baryonic mass components in galaxy clusters I: Mass constraints from Abell S1063. arXiv e-prints, 2509–07762 (2025) arXiv:2509.07762 [astro-ph.GA]

[14] Bacon, R., Accardo, M., Adjali, L., Anwand, H., Bauer, S., Biswas, I., Blaizot, J., Boudon, D., Brau-Nogue, S., Brinchmann, J., Caillier, P., Capoani, L., Carollo, C.M., Contini, T., Couderc, P., Daguisé, E., Deiries, S., Delabre, B., Dreizler, S., Dubois, J., Dupieux, M., Dupuy, C., Emsellem, E., Fechner, T., Fleischmann, A., François, M., Gallou, G., Gharsa, T., Glindemann, A., Gojak, D., Guiderdoni, B., Hansali, G., Hahn, T., Jarno, A., Kelz, A., Koehler, C., Kosmalski, J., Laurent, F., Le Floch, M., Lilly, S.J., Lizon, J.-L., Loupias, M., Manescau, A., Monstein, C., Nicklas, H., Olaya, J.-C., Pares, L., Pasquini, L., Pécontal-Rousset, A., Pelló, R., Petit, C., Popow, E., Reiss, R., Remillieux, A., Renault, E., Roth, M., Rupprecht, G., Serre, D., Schaye, J., Soucail, G., Steinmetz, M., Streicher, O., Stuik, R., Valentin, H., Vernet, J., Weilbacher, P., Wisotzki, L., Yerle, N.: The MUSE second-generation VLT instrument. In: McLean, I.S., Ramsay, S.K., Takami, H. (eds.) Ground-based and Airborne Instrumentation for Astronomy III. Society of Photo-Optical Instrumentation Engineers (SPIE) Conference Series, vol. 7735, p. 773508 (2010)

[15] Cappellari, M.: Full spectrum fitting with photometry in `pPXF`: stellar population vs. dynamical masses, non-parametric star formation history and metallicity for 3200 lega-c galaxies at redshift $z \sim 0.8$. Monthly Notices of the Royal Astronomical Society **526**(3), 3273–3300 (2023)

[16] Cappellari, M.: Improving the full spectrum fitting method: accurate convolution with Gauss-Hermite functions. Monthly Notices of the Royal Astronomical Society **466**(1), 798–811 (2017) arXiv:1607.08538 [astro-ph.GA]

[17] Montes, M., Trujillo, I.: Intracluster light at the frontier. ii. the frontier fields

clusters. Monthly Notices of the Royal Astronomical Society **474**(1), 917–932 (2018)

[18] Marini, I., Borgani, S., Saro, A., Granato, G.L., Ragone-Figueroa, C., Sartoris, B., Dolag, K., Murante, G., Ragagnin, A., Wang, Y.: Velocity dispersion of brightest cluster galaxies in cosmological simulations. Monthly Notices of the Royal Astronomical Society **507**(4), 5780–5795 (2021) arXiv:2109.00223 [astro-ph.GA]

[19] Butler, J., Martin, G., Hatch, N.A., Pearce, F., Brough, S., Dubois, Y.: Intracluster light is a biased tracer of the dark matter distribution in clusters. Monthly Notices of the Royal Astronomical Society **539**(3), 2279–2291 (2025) arXiv:2504.03518 [astro-ph.GA]

[20] Morishita, T., Abramson, L.E., Treu, T., Schmidt, K.B., Vulcani, B., Wang, X.: Characterizing Intracluster Light in the Hubble Frontier Fields. The Astrophysical Journal **846**(2), 139 (2017) arXiv:1610.08503 [astro-ph.GA]

[21] Brough, S., Ahad, S.L., Bahé, Y.M., Ellien, A., Gonzalez, A.H., Jiménez-Teja, Y., Kimmig, L.C., Martin, G., Martínez-Lombilla, C., Montes, M., Pillepich, A., Ragusa, R., Remus, R.-S., Collins, C.A., Knapen, J.H., Mihos, J.C.: Preparing for low surface brightness science with the Vera C. Rubin Observatory: a comparison of observable and simulated intracluster light fractions. Monthly Notices of the Royal Astronomical Society **528**(1), 771–795 (2024) arXiv:2311.18016 [astro-ph.CO]

[22] Stone, C.J., Courteau, S., Arora, N., Jarrett, T.H.: Autoprof: Automated galaxy photometry pipeline. The Astrophysical Journal Supplement Series **253**(2), 44 (2021)

[23] Shen, S., Mo, H.J., White, S.D.M., Blanton, M.R., Kauffmann, G., Voges, W., Brinkmann, J., Csabai, I.: The size distribution of galaxies in the Sloan Digital Sky Survey. Monthly Notices of the Royal Astronomical Society **343**(3), 978–994 (2003) arXiv:astro-ph/0301527 [astro-ph]

[24] Holden, B.P., Franx, M., Illingworth, G.D., Postman, M., van der Wel, A., Kelson, D.D., Blakeslee, J.P., Ford, H., Demarco, R., Mei, S.: The Ellipticities of Cluster Early-type Galaxies from z ~1 to z ~0: No Evolution in the Overall Distribution of Bulge-to-Disk Ratios. The Astrophysical Journal **693**(1), 617–633 (2009) arXiv:0811.1986 [astro-ph]

[25] Gassis, R., Bayliss, M.B., Sharon, K., Mahler, G., Gladders, M.D., McDonald, M., Dahle, H., Florian, M.K., Rigby, J.R., Elicker, L.A., Owens, M.R., Adhikari, P., Khullar, G.: Tracing Structure: Shape and Centroid Deviations in 39 Strong Lensing Clusters as a Test of Cluster Formation Predictions. arXiv e-prints, 2511–22661 (2025) arXiv:2511.22661 [astro-ph.CO]

[26] Fernandez, A., et al. in prep. (2025)

[27] Navarro, J.F., Frenk, C.S., White, S.D.M.: The Structure of Cold Dark Matter Halos. The Astrophysical Journal **462**, 563 (1996) arXiv:astro-ph/9508025 [astro-ph]

[28] Harvey, D., Revaz, Y., Schaller, M., Schneider, A., Tregidga, E., Vecchi, F.: DARKSKIES: A suite of super-sampled zoom-in simulations of galaxy clusters with self-interacting dark matter. arXiv e-prints, 2509–19842 (2025) arXiv:2509.19842 [astro-ph.CO]

[29] Karman, W., Caputi, K.I., Grillo, C., Balestra, I., Rosati, P., Vanzella, E., Coe, D., Christensen, L., Koekemoer, A.M., Krühler, T., Lombardi, M., Mercurio, A., Nonino, M., van der Wel, A.: MUSE integral-field spectroscopy towards the Frontier Fields cluster Abell S1063. I. Data products and redshift identifications. Astronomy & Astrophysics **574**, 11 (2015) arXiv:1409.3507 [astro-ph.GA]

[30] Karman, W., Caputi, K.I., Caminha, G.B., Gronke, M., Grillo, C., Balestra, I., Rosati, P., Vanzella, E., Coe, D., Dijkstra, M., Koekemoer, A.M., McLeod, D., Mercurio, A., Nonino, M.: MUSE integral-field spectroscopy towards the Frontier Fields cluster Abell S1063. II. Properties of low luminosity Lyman α emitters at $z > 3$. Astronomy & Astrophysics **599**, 28 (2017) arXiv:1606.01471 [astro-ph.GA]

[31] Lotz, J.M., Koekemoer, A., Coe, D., Grogin, N., Capak, P., Mack, J., Anderson, J., Avila, R., Barker, E.A., Borncamp, D., Brammer, G., Durbin, M., Gunning, H., Hilbert, B., Jenkner, H., Khandrika, H., Levay, Z., Lucas, R.A., MacKenty, J., Ogaz, S., Porterfield, B., Reid, N., Robberto, M., Royle, P., Smith, L.J., Storrie-Lombardi, L.J., Sunnquist, B., Surace, J., Taylor, D.C., Williams, R., Bullock, J., Dickinson, M., Finkelstein, S., Natarajan, P., Richard, J., Robertson, B., Tumlinson, J., Zitrin, A., Flanagan, K., Sembach, K., Soifer, B.T., Mountain, M.: The Frontier Fields: Survey Design and Initial Results. The Astrophysical Journal **837**(1), 97 (2017) arXiv:1605.06567 [astro-ph.GA]

[32] Cappellari, M., Copin, Y.: Adaptive spatial binning of integral-field spectroscopic data using voronoi tessellations. Monthly Notices of the Royal Astronomical Society **342**(2), 345–354 (2003)

[33] Knowles, A.T., Sansom, A.E., Vazdekis, A., Allende Prieto, C.: smiles ssps: a library of semi-empirical miles stellar population models with variable [α/fe] abundances. Monthly Notices of the Royal Astronomical Society **523**(3), 3450–3470 (2023)

[34] Montes, M., Trujillo, I.: Stellar populations of the intracluster light in the hubble frontier fields. The Astrophysical Journal **794**(2), 137 (2014)

[35] Edwards, L.O.V., Alpert, H.S., Newman, A.B., Trentham, N., Sand, D.J., Belli, S., Smith, R.J.: Clocking the formation of today's largest galaxies: wide-field integral spectroscopy of brightest cluster galaxies and their surroundings. Monthly Notices of the Royal Astronomical Society **491**(2), 2617–2635 (2020)

[36] Barbosa, C.E., *et al.*: Stellar populations and kinematics in bcg halos. Astronomy and Astrophysics **649**, 25 (2021)

[37] Gu, M., Conroy, C., Brammer, G.: Coordinated Assembly of Brightest Cluster Galaxies. The Astrophysical Journal Letters **862**(2), 18 (2018) arXiv:1805.04520 [astro-ph.GA]